Seeking non-Fourier heat transfer with ultrabroad band thermoreflectance spectroscopy

Ahmad Zenji, Gilles Pernot, David Lacroix, Jean-Michel Rampnoux, Olivier Bourgeois, Stéphane Grauby, Stefan Dilhaire

communications materials

Article

https://doi.org/10.1038/s43246-024-00572-7

Seeking non-Fourier heat transfer with ultrabroad band thermoreflectance spectroscopy

Ahmad Zenji[1], Gilles Pernot[2], David Lacroix[2], Jean-Michel Rampnoux[1], Olivier Bourgeois[3], Stéphane Grauby[1] ✉ & Stefan Dilhaire[1] ✉

Studying superdiffusive thermal transport is crucial for advanced thermal management in electronics and nanotechnology, ensuring devices run efficiently and reliably. Such study also contributes to the design of high-performance thermoelectric materials and devices, thereby improving energy efficiency. This work leads to a better understanding of fundamental physics and non-equilibrium phenomena, fostering innovations in numerous scientific and engineering fields. We are showing, from a one shot experiment, that clear deviations from classical Fourier behavior are observed in a semiconductor alloy such as InGaAs. These deviations are a signature of the competition that takes place between ballistic and diffusive heat transfers. Thermal propagation is modelled by a truncated Lévy model. This approach is used to analyze this ballistic-diffusive transition and to determine the thermal properties of InGaAs. The experimental part of this work is based on a combination of time-domain and frequency-domain thermoreflectance methods with an extended bandwidth ranging from a few kHz to 100 GHz. This unique wide-bandwidth configuration allows a clear distinction between Fourier diffusive and non-Fourier superdiffusive heat propagation in semiconductor materials. For diffusive processes, we also demonstrate our ability to simultaneously measure the thermal conductivity, heat capacity and interface thermal resistance of several materials over 3 decades of thermal conductivity.

Thin films were found to have widespread applications in engineering systems to enhance their optical, electrical, and thermal properties. However, when the thickness of a thin film becomes smaller than the mean free path of its heat carriers (such as electrons or phonons), the thermal behavior of the film significantly deviates from its bulk counterpart due to geometric constraints. This thermal transitional region, known as the intermediate regime, lies between ballistic flight and purely diffusive transport behaviors. This intermediate regime is clearly related to the spectral dependence of the phonon spectrum, and is characterized by a superdiffusive regime which can be described by the Lévy Walks theory[1,2]. This superdiffusive behavior, distinct from conventional Brownian motion, is also expected in various semiconducting alloys, and in particular in InGaAs. Gaining a comprehensive understanding of this superdiffusive thermal transport is vital for numerous technological applications, such as those dealing with nanoelectronic devices, heat management and thermoelectric materials. It is also of crucial importance in active and optoelectronic devices which have often heat sources in the InGaAs material layer.Recently, another phonon transport mechanism, namely the hydrodynamic heat transport, not addressed in this work, has been investigated in several works[3–5] and applied to Frequency Domain ThermoReflectance (FDTR) measurements[6]. In the particular case of low temperature in silicon, it appears that a model that takes into account hydrodynamic component of phonon motion is necessary to accurately fit amplitude and phase recorded thermal signal. In 2007, Koh and Cahill[7] conducted femtosecond laser Time-Domain ThermoReflectance (TDTR) experiments, where they observed an anomalous frequency dependence of the thermal conductivity in semiconductor alloys. When a modulated heat source generated by laser pulses oscillates above the MHz range, they observed that the apparent thermal conductivity of alloys decreases by over 50% when compared to its bulk value while the apparent thermal conductivity remains constant in pure crystals (such as InP, GaAs) and amorphous materials (like SiO_2). The authors claimed that ballistic phonons, with a mean free path longer than the thermal diffusion length of

[1]Université de Bordeaux, LOMA, CNRS UMR 5798, F-33400 Talence, France. [2]Université de Lorraine, CNRS, LEMTA, Nancy, F-54000, France. [3]Institut NEEL, CNRS, Université de Grenoble Alpes, Grenoble, F-38042, France. ✉e-mail: stephane.grauby@u-bordeaux.fr; stefan.dilhaire@u-bordeaux.fr

the heat source do not contribute to the measured thermal conductivity. However, their cumulative approach[8] inherently carried a bias since it maintained a diffusive-Fourier regime. Consequently, their TDTR experiment was converted into a method for measuring the mean free path spectrum of phonons[9,10]. In 2010, Siemens et al.[11] used a soft X-Ray TDTR experiment to observe deviation in Fourier predictions while varying the size of metallic heaters from 65 nm to 2 µm. Soft X-Ray features drastically increased the spatial resolution of their experiment and allowed the authors to observe a ballistic-diffusive transition. They tempered this effect by assuming an additional ballistic boundary resistance between the heater and its medium, but once again, their theoretical approach was Fourier based. In 2015, Nelson and Minnich[12,13] conducted experimental measurements using a Transient Thermal Grating (TTG) technique and presented a similar anomalous behavior of thermal conductivity with a spatially modulated heat source. Their method involved the absorption of crossed laser pulses, which established a sinusoidal temperature profile. The temperature-induced index grating diffraction of a probe laser beam was used to monitor the temperature distribution. By adjusting the period of the thermal grating, the heat penetration length could be varied within the range of 1–10 µm. At small spatial periods corresponding to a high-frequency excitation, a reduction in the apparent thermal conductivity was observed, indicating a transition from the diffusive to the ballistic transport regime. Again, this behavior was explained by the authors considering that only phonons with a mean free path shorter than the size of the heat source contribute significantly to the thermal conductivity.Indeed, the observed frequency dependence of thermal conductivity in thermoreflectance experiments arises from a bias that occurs when a purely diffusive-Fourier model fails to account for the transition between the diffusive and ballistic regimes. In 2015, Vermeersch et al.[14] demonstrated, through first-principle calculations and solving the Boltzmann transport equation, that a quasi-ballistic transition regime often emerges in alloys. To describe this regime, they introduced a new model based on Lévy dynamics[1,2], which played a crucial role in understanding the ballistic-diffusive effects. In their study, Lévy dynamics in alloys is referred to as super-diffusion[15].

The results obtained by Vermeersch et al. revealed that the previously mentioned reductions in apparent conductivity observed in semiconductor alloys are a direct manifestation of superdiffusive Lévy transport, without having to assume a frequency-dependent thermal conductivity. Moreover, the formalism indicated that the transient temperature behavior within the material significantly deviates from the Fourier theory, offering improvements in the thermal characterization of alloys and material interfaces. Such experimental measurements obtained with a classical TDTR setup[7] have enabled to highlight a superdiffusive regime but this kind of experiment has inherent drawbacks which complicate the analysis such as cumulative thermal effects or a limited acquisition time window. One new experimental evidence of superdiffusive transport was reported in 2022[16]. Nevertheless, the process described by the authors needs i) to grow more than 10 samples with thicknesses from 10 nm up to 1 µm, ii) to perform measurements from ambient temperature down to cryogenic. In addition, the 3-omega method used in this article only allows measuring a sample thermal resistance. There is no possibility to know the value of the frequency range of the phonons involved without varying the sample thickness.

In the following work, we will delve into the origin and principles of the super-diffusion regime and explore its modeling in greater detail. From an experimental aspect, ultra wideband thermal spectroscopy associated to Levy modeling is a unique tool for instantly revealing the presence of superdiffusion processes and identifying the frequency range of the phonons that contribute the most to the non-Fourier process. The key advantages of this technique are as follows: a single sample is sufficient and it is not necessary to carry out a temperature study. The super diffusive regime is then highlighted in a one shot experiment.

Thermal spectroscopy combined with a probabilistic approach to phonon distribution sheds a new light on thermal transport.

Results and discussion

Theoretical background

This section summarizes the approach described in ref. 14, providing a framework for fitting and predicting the experimental data. It also justifies the necessity to develop an ultrabroad band experimental technique, described in the next section, in order to demonstrate the non-Fourier behavior. Classically the formalism is rooted in a probabilistic framework, where the movement of thermal energy carriers within the material is characterized as a stochastic process. This approach utilizes the duality between the temperature response $\Delta T(\mathbf{r},t)$ and the probability density function $P(\mathbf{r},t)$ of encountering a randomly moving energy carrier at position $\mathbf{r}$ and time t. This duality is expressed as $\Delta T(\mathbf{r},t) \Longleftrightarrow \frac{P(\mathbf{r},t)}{\rho C}$, where ρ and C respectively stand for the density and the specific heat of the medium. In essence, we employ continuous time random walk (CTRW) processes, which involve a series of transition events[17,18], to describe the behavior of thermal energy carriers.

Regular one dimensional (1D) Fourier diffusion is stochastically equivalent to Brownian motion[15] where a single pulse $Q \times \delta(t)$ of surface energy density (in $J.m^{-2}$) is expressed with the probability distribution:

$$\Delta T_{1D}(x,t) = \frac{Q}{\rho C} P_{1D}(x,t) \tag{1}$$

with $P_{1D}(x,t) = \frac{1}{\sqrt{4\pi Dt}} e^{-\frac{x^2}{4Dt}}$ where D is the thermal diffusion coefficient and $\int_{-\infty}^{+\infty} P_{1D}(x,t)dx = 1$.

In the spatial Fourier domain, the temperature distribution becomes:

$$\Delta T_{1D}(\xi,t) = \frac{Q}{\rho C} P_{1D}(\xi,t) = \frac{Q}{\rho C} e^{-\xi^2 Dt} \tag{2}$$

While in the double transformed Fourier-Laplace domain the expression becomes:

$$\Delta T_{1D}(\xi,s) = \frac{Q}{\rho C} P_{1D}(\xi,s) = \frac{Q}{\rho C} \times \frac{1}{s+\xi^2 D} \tag{3}$$

$P_{1D}(\xi,s)$ represents the characteristic function of a normalized random-walk process. In this context, $P_{1D}(x,t)dx$ denotes the probability of locating the injected source energy within the range $[x, x+dx]$ at time t. The derivatives of $P_{1D}(\xi,s)$ with respect to ξ exhibit continuity at $\xi = 0$, implying that the moments of $P_{1D}(x,t)$ exist and are finite.

For a more general non diffusive process the formalism remains unchanged, but the probability distribution is modified in the following way[17]:

$$P_{1D}(\xi,s) = \frac{1}{s+\psi(\xi)} \tag{4}$$

with $\psi(\xi) = D_\alpha |\xi|^a$

The $\xi^2 D$ pole in Eq. (3) in the Laplace domain is replaced in Eq. (4) by a function of the wave number $\psi(\xi)$ from which we deduce a fractional diffusive coefficient $D = \frac{\psi(\xi)}{\xi^2} = D_\alpha |\xi|^{\alpha-2}$.

The flaw of such an approach is that only one regime can be described depending on the exponent value $\alpha\,(1 < \alpha \leq 2)$. If $\alpha = 2$ then propagation is purely diffusive while if $\alpha < 2$ the propagation is superdiffusive. A more complete description is needed when a large time scale is accessible to the measurement implying a corresponding large scale of frequencies (s) and wave numbers (ξ). The probability distribution is modified and the $\psi(\xi)$ function is rewritten as follows[19]:

$$\psi(\xi) = -\frac{2D\xi_{bd}^2}{\alpha(\alpha-1)} \cdot \left(\left(\left(\frac{\xi}{\xi_{bd}} \right)^2 + 1 \right)^{\frac{\alpha}{2}} cos\left(\alpha.arctan\left(\frac{\xi}{\xi_{bd}} \right) \right) - 1 \right) \tag{5}$$

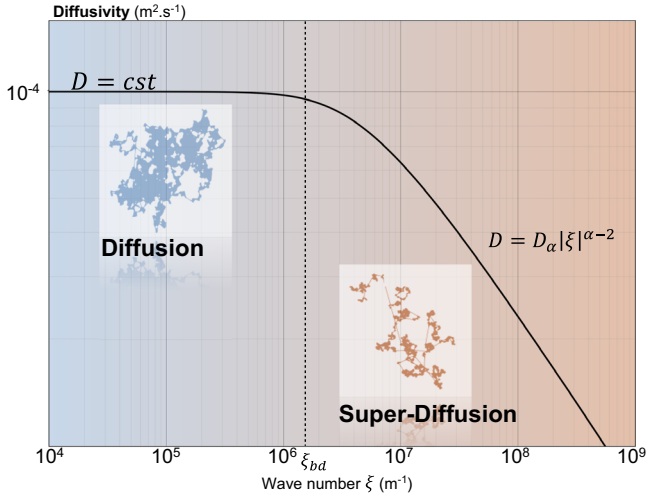

Fig. 1 | Diffusivity $\frac{\psi(\xi)}{\xi^2}$ vs wave numbers in log-log scale. At low spatial frequencies the diffusivity appears constant as the propagation is purely diffusive. At high spatial frequencies, above the cut-off, the transport becomes purely superdiffusive with a α-2 exponent.

This expression comes from the truncated Levy distribution formalism able to describe both purely diffusive Fourier process and superdiffusive Levy carriers. α is the superdiffusive exponent and ξ_{bd} the truncation wave number such as $\xi_{bd} = \frac{2\pi}{u_{bd}}$ of the Levy distribution where the truncation appears through u_{bd} (the bd index stands for the ballistic-diffusive transition) u_{bd} is the value of the jump cut-off[20] so that the mean square displacement (MSD) could be finite and regulates the length over which the transition from quasi-ballistic to diffusive transport occurs[19]. The function $\frac{\psi(\xi)}{\xi^2}$ is plotted in Fig. 1 for the following parameters: $u_{bd} = 4\,\mu m$, $D = 10^{-4}\,m^2.s^{-1}$ et $\alpha = 1.5$. The Fourier regime clearly appears at low spatial frequencies while the highest frequencies evidence the superdiffusive propagation. The transition between the two regimes appears for $\xi = \xi_{bd} = 1.6 \times 10^6 m^{-1}$. Considering the truncation parameter u_{bd} being equal to the diffusion length, we can deduce the $f_{cut-off}$ cut-off frequency between the two transport regimes:

$$\frac{2\pi}{\xi_{bd}} = u_{bd} = L_{Dmin} = \sqrt{\frac{D}{\pi f_{cut-off}}} \tag{6}$$

$$f_{cut-off} = \frac{D\xi_{bd}^2}{4\pi^3} = 2.0\text{MHz} \tag{7}$$

This value depending on the material thermal diffusivity and on the jump cut-off value, the cut-off frequency is expected to appear in the [1 MHz, 1 GHz] range[14].

From these considerations we now have a complete analytical expression for 1D energy density single pulse response in the material in the Fourier-Laplace domain from which we can calculate the response $P_{1D}(x,t)$ in the real space by classical numerical Fourier inverse Transforms. The extension to the 3D solution is obtained assuming an isotropic propagation and from symmetry arguments[19]:

$$\Delta T_{3D}(r,t) = \frac{2}{\rho C} P_{1D}^3(x = r/\sqrt{3}, t) \tag{8}$$

with r the distance to the source.

Ultrabroad band thermoreflectance spectroscopy

Given the frequency range of the expected superdiffusive regime, there is a need for a spectroscopy method with high sensitivity in the [1 MHz, 1 GHz] region.

Femtosecond pump-probe thermoreflectance[21,22] has proven to be a very adequate and efficient method to assess the dynamics of electron and phonon transport in nanomaterials and to characterize nanomaterial properties such as thermal properties[23–27] or acoustic and optical properties[28–30]. In such pump-and-probe experiments, a metallic film, usually aluminum or gold, is deposited on the sample layer to increase absorption and convert pump light into heat. The high-intensity pump heats the sample and the low-intensity probe senses its reflectivity response. Femtosecond laser sources can then be used with this kind of pump-probe set-up to investigate the thermal properties of thin films, multilayers, and nano-objects, and to determine thermal interface resistances[25–27,31]. They provide the very high temporal resolution required to study small spatial dimensions with a good dynamic range. We can distinguish two configurations, namely TDTR[32–36] and FDTR[37–40], for which the reflectivity variations are respectively measured either as a function of time or as a function of frequency (see Supplementary Figs. S1.1 and S1.2).

It is clear that none of the spectral ranges of the TDTR and FDTR techniques are suitable to bring out the superdiffusive regime which is expected to appear in the [1 MHz, 1 GHz] frequency range. In this frequency range, we have checked that, with a 70 nm thick Al transducer, we do not have to take into account the non-equilibrium electron contribution (see Supplementary Fig. S2.2). We have then combined both techniques to obtain a broadband thermal spectral sensor. The FDTR and TDTR experiments respectively probe [10 kHz, 200 MHz] and [76 MHz, 1 THz] frequency ranges which finally lead to a [10 kHz, 1 THz] final range. Several precautions must be taken in order for measurements obtained by both methods to overlap. In particular, the same magnification conditions, and the same pump and probe wavelengths must be used in both setups. In addition, since the magnitude signal is dependent on the energy absorbed within the sample, the use of the same pump power should be guaranteed unless the thermal analysis is made from the phase signal. Indeed, this phase signal can then be used to identify the thermal properties of the samples studied, after compensating for optical path differences and propagation delays.

To validate this ultra-wide thermal spectroscopy, experimental measurements were carried out first on a silicon sample. For these measurements, the radius size of the pump and probe beams were measured to be respectively 6.5 µm and 4.5 µm. The silicon substrate is covered by a 70-nm thick Al transducer. The amplitude and phase signals of the FDTR/TDTR sensor are presented in Fig. 2 where we can note a perfect overlap of the TDTR and FDTR measurements, as well as in the amplitude and in the phase curves in the [76 MHz, 200 MHz] region.

Modeling and parameter identification

From the phase curve, next step consists in identifying the thermal properties of the sample from the measurement. A 1TM (Fourier One Temperature Model)[41,42] is used to describe the heat transfer during a pump-probe experiment. The sample is modeled by an Al transducer layer deposited on a semi-infinite substrate as presented in the central part of Fig. 3. The discontinuity of the temperature field at the interface is modeled by an interface resistance. In this section, for simplicity, we have assumed that the transducer is instantaneously thermalized in both models in order to focus on the material of interest.

At this point, we can compute both temperatures on top of the transducer (where the probe laser is performing the temperature measurement) and on top of the material of interest (where the superdiffusive effect is expected to be observable) using the quadruple formalism[42] in the Fourier ($t \to \omega$) Hankel ($r \to \lambda$) domains and assuming that the heat is being

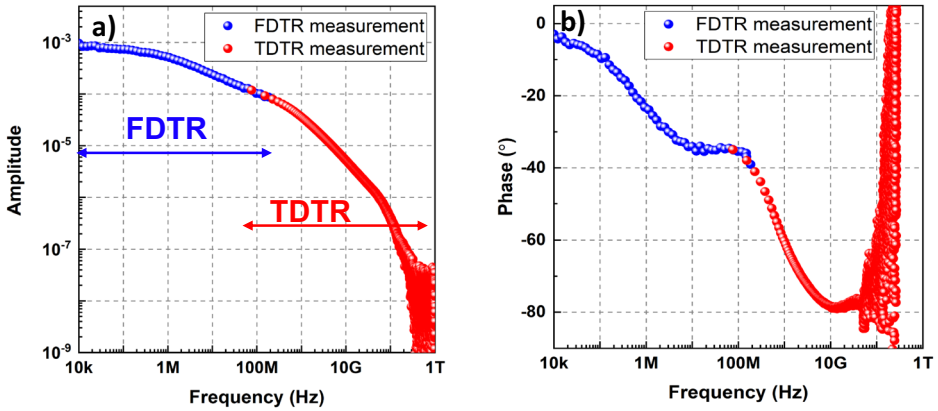

Fig. 2 | Ultrabroad Band TR on a Al/Si sample through FDTR/TDTR combined measurements. **a** Amplitude and **b** phase spectral response on an Al/Si sample measured by the FDTR/TDTR ultra-wide thermal spectroscopy.

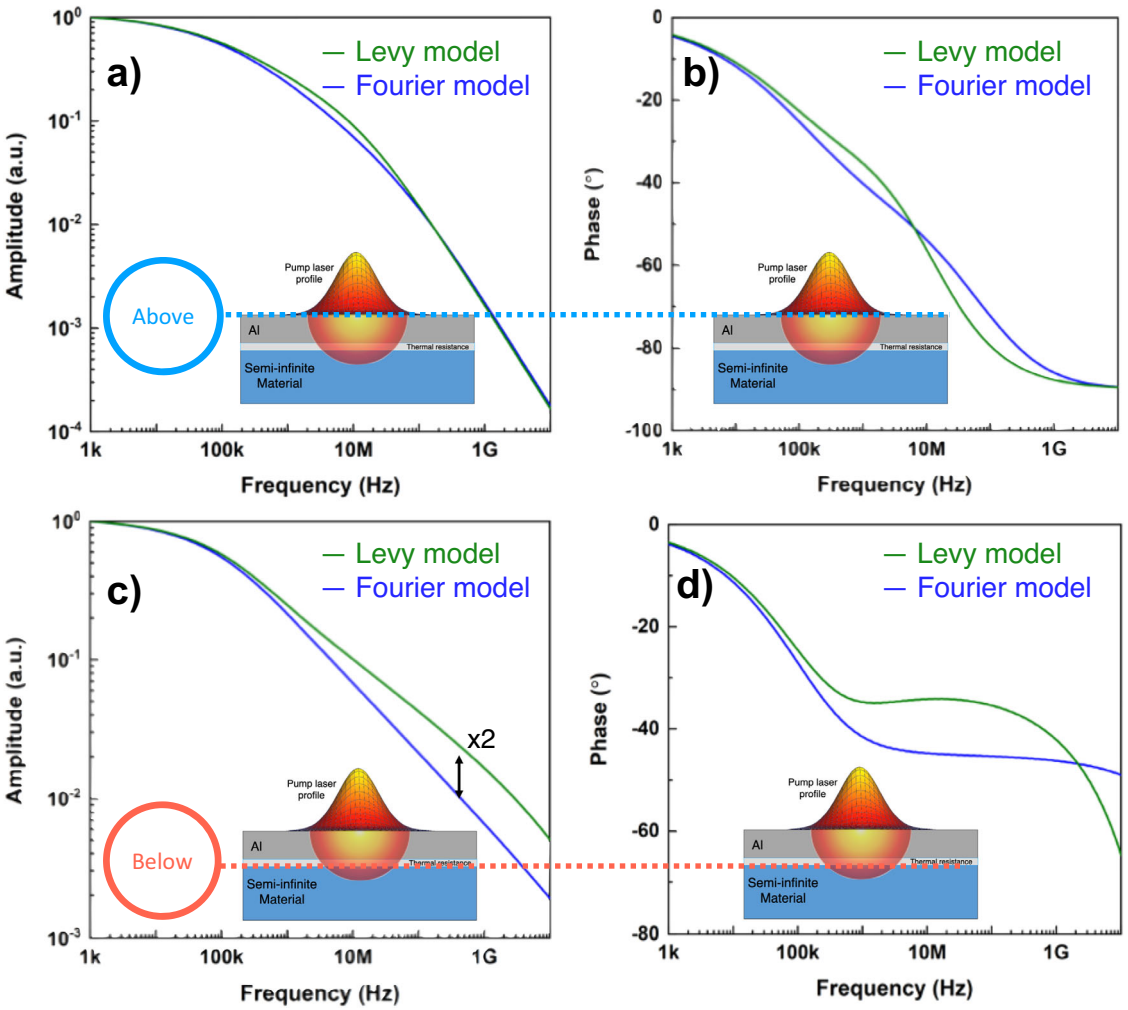

Fig. 3 | Screening effect of the transductor. Comparison of modeled amplitude and phase Fourier and truncated Lévy spectra above the transducer (**a** for the amplitude and **b** for the phase) and below the transducer (**c** for the amplitude and **d** for the phase) for a semi-infinite material. The thermal properties used for the calculation are shown in Table 1.

deposited by a spatial Gaussian shape single laser pulse of energy Q.

$$\begin{bmatrix} T_1(\lambda,\omega) \\ Q(\lambda) \end{bmatrix} = \begin{bmatrix} 1 & 0 \\ k_{Al}t_{Al}(\frac{j\omega}{D_{Al}}+\lambda^2) & 1 \end{bmatrix} \cdot \begin{bmatrix} 1 & R \\ 0 & 1 \end{bmatrix} \cdot \begin{bmatrix} T_2(\lambda,\omega) \\ T_2(\lambda,\omega).Z^{-1}(\lambda,\omega) \end{bmatrix} \quad (9)$$

Q stands for the energy of the laser absorbed by the aluminum transducer with a thickness t_{Al} and respectively a thermal conductivity and diffusivity k_{Al} and D_{Al}. R is the thermal resistance interface between the transducer and the layer of interest. $Z(\lambda, \omega)$ is the thermal impedance of the material under study considered as a semi-infinite medium. T_1 is the surface temperature measured by the probe beam while T_2 is the temperature on top of the layer of interest. $T_1(\omega) = T(z = 0, \omega)$ and $T_2(\omega) = T(z = t_{Al}, \omega)$ are obtained solving numerically this system of two equations.

Table 1 | Physical properties of the different layers and interface used for the calculations shown in Fig. 3

Al transducer	Thickness	70 nm
	Thermal conductivity	180 $W.m^{-1}.K^{-1}$
	Specific heat capacity	2.45 MJ. $m^{-3}.K^{-1}$
Interface	Thermal resistance	$R_{Al/Si}$ = 5 $nK.m^2.W^{-1}$
Semi-infinite substrate	Thermal conductivity	k_{Sub} = 10 $W.m^{-1}.K^{-1}$ (Fourier) k_{Sub} = 10 $W.m^{-1}.K^{-1}$; α = 1.5; u_{BD} = 4 µm (Levy)
	Specific heat capacity	$\rho C_{Substrate}$ = 1.65 MJ. $m^{-3}.K^{-1}$

In a classical Fourier diffusive regime, the impedance is given by $Z_{Fourier}(\lambda,\omega) = (k\sqrt{\frac{j\omega}{D}+\lambda^2})^{-1}$ while in a superdiffusive Lévy regime, it must be modified calculating the Lévy impedance through the Green's function in the Fourier-Hankel domain[19]:

$$Z_{Lévy}(\lambda,\omega) = \frac{\int_{-\infty}^{\infty}\int_{0}^{\infty}\Delta T_{3D}(r,t)e^{-j2\omega t}J_0(\lambda r)rdrdt}{Q(\lambda)} \quad (10)$$

where $\Delta T_{3D}(r,t)$ is given by Eq. (8).

Consequently, a comparative study of the Lévy model thermal response with that of the Fourier-1TM can be carried out to show the difference between these two models. Figure 3 shows the amplitude and spectral phase of the thermal response calculated with the Fourier-1TM and Lévy models of a semi-infinite substrate covered with a 70 nm aluminum transducer at two specific positions: first (lower part of Fig. 3) at the interface between the Al layer and the semi-infinite material of interest, second (upper part of Fig. 3) on top of the metal surface where the temperature is measured by thermoreflectance. The thermal properties used in the calculation are shown in Table 1.

We have verified that the Lévy model becomes a regular Fourier model with $\alpha = 2$, giving the same spectral response as the one calculated by the Fourier Model (this result is not shown in the graph for the sake of clarity). However, when the exponent α is equal to 1.5, the Lévy model behaves differently from the Fourier model, showing superdiffusive effects. Both amplitude and phase display an evident signature of the superdiffusive nature of the thermal transport but since the thermal phase does not require a normalization process, it can be directly compared with the experimental signal. This is one of the reasons why, in the following of this work, we shall focus on the thermal phase to study the non-Fourier thermal transport.

The differences between both models are very pronounced on the surface of the material below the transducer. The Fourier model underestimates the temperature amplitude rise of the hot spot under the surface by a factor of two at high frequencies, i.e. at short times when ballistic effects are prevalent as ballistic phonons do not contribute to cooling mechanisms[7]. The phase is also strongly influenced by the nature of the propagation phenomenon (Lévy or Fourier).

The transducer evens out the temperature distribution and masks non-diffusive effects when viewed from the sample surface, in particular in the amplitude response. Nevertheless, super-diffusion is still visible from above the transducer over two decades around 10 MHz in the phase response. Indeed, the 1TM and superdiffusive ($\alpha = 1.5$) models behave identically at high frequency, where the thermal response is sensitive to the transducer. Since the transducer is considered to be instantaneously thermalized, the phase of the spectral response tends towards −90° at high frequency. However, at low frequencies, both model phase responses are superimposed and tend towards 0° due to the semi-infinite medium. The differences in the rest of the frequency range are due to the superdiffusive regime. Therefore, the range of this thermal regime is accessible by the FDTR/TDTR thermoreflectance spectral sensor. In addition to the FDTR/TDTR overlapping conditions and the lack of normalization necessity, this is another reason to use the phase signal to perform the thermal parameter identification rather than the amplitude signal.

Customarily[36], a 70-nm thick transducer is used as the best compromise between thermal transparency and the best energy deposition efficiency by the pump laser. It is under these conditions that we have been able to experimentally demonstrate the super-diffusion in the last section.

We have used the model presented above to identify thermal parameters of pure semiconductor crystals such as Si and Ge, amorphous SiO_2, polymers and finally, a semiconductor alloy InGaAs where non-diffusive Lévy effects are expected.

Table 2 | Physical properties of the different layers and interface

Al transducer	Thickness	70 nm
	Thermal conductivity	180 $W.m^{-1}.K^{-1}$
	Specific heat capacity	2.45 MJ. $m^{-3}.K^{-1}$
Interface	Thermal resistance*	$R_{Al/Si}$ = 2.3 $nK.m^2.W^{-1}$
Si substrate	Thermal conductivity*	k_{Si} = 135 $W.m^{-1}.K^{-1}$
	Specific heat capacity*	ρC_{Si} = 1.69 MJ. $m^{-3}.K^{-1}$

The * stands for identified free parameters in the model.

Diffusive transport in Fourier material

The identification was carried out on the silicon sample whose thermoreflectance signals were previously presented in Fig. 2. Table 2 summarizes the known Al properties (thickness, penetration depth, thermal conductivity, and specific heat capacity) and the three properties to be identified with the corresponding identified values.

A sensitivity study of the 1TM model (see Supplementary Fig. S3) shows that, for materials with a thermal conductivity higher than 10 $W.m^{-1}.K^{-1}$, thanks to the ultrabroad bandwidth of the experimental measurements, the interfacial thermal resistance can be simultaneously identified along with the substrate thermal conductivity and specific heat capacity. For lower thermal conductivities, between 1 and 10 $W.m^{-1}.K^{-1}$, the two latter parameters are correlated, then only both interfacial thermal resistance and material thermal conductivity can be identified.

Finally for very low thermal conductivities ($k < 1$ $W.m^{-1}.K^{-1}$), the thermal contact resistance R_k may be much smaller than the sheet resistance of volume probed beneath the surface L_D/k (where L_D is the thermal diffusion length): $\frac{L_D}{k} \gg R_k$. As the thermal flux crosses these resistances in series, when one is much higher than the other, the lower resistance has no influence on thermal transport and cannot be estimated. In our case the sensitivity to R_k is very weak making its identification impossible. That is the reason why only the thermal conductivity has been identified.

Figure 4 shows the experimental phase response and the theoretical 1TM optimization curve for the Al/Si sample, characteristic of a classical Fourier thermal transport[6,43]. The best optimization was obtained for the following parameters: k_{Si} = 135 $W.m^{-1}.K^{-1}$, ρC_{Si} = 1.69 $MJ.m^{-3}.K^{-1}$ and $R_{Al/Si}$ = 2.3 $nK.m^2.W^{-1}$, which are close to the values found in literature[44,45].

In addition, 5 other materials with different thermal conductivities ranging from 0.2 to 16.4 $W.m^{-1}.K^{-1}$ were measured: germanium-manganese (GeMn), scandium nitride (ScN), vanadium dioxide (VO_2), silica (SiO_2) and a polymer (PI). The phase experimental responses and the 1TM optimization theoretical curves for these materials are given in the Supplementary Figs. S4.1–S4.5. Figure 5 presents a comparison between the identified values for the 6 materials and the values found in the literature[44–49].

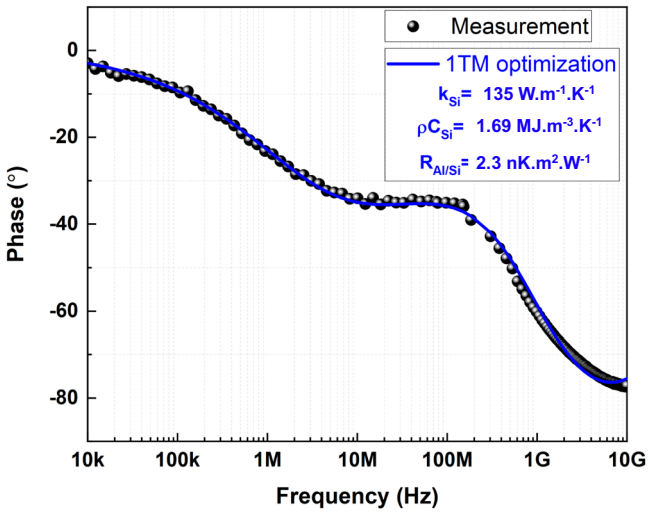

Fig. 4 | Thermal properties identification. Phase signal measured by the FDTR/TDTR sensor on a Al/Si sample and best 1TM fit.

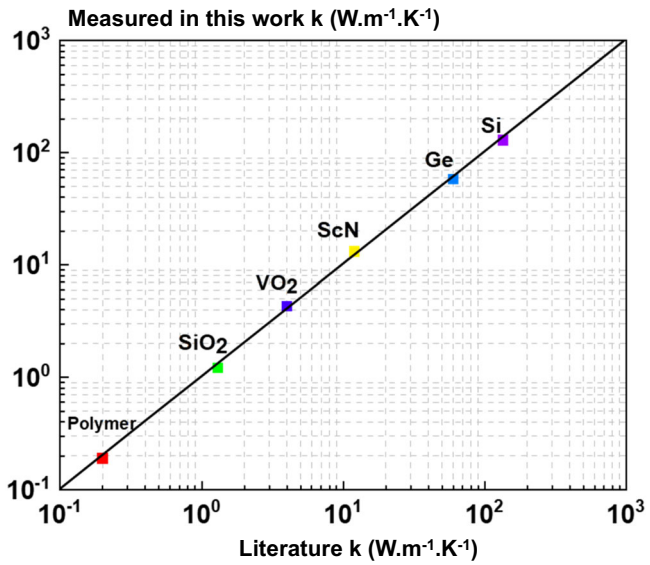

Fig. 5 | Range of thermal conductivity measurements. Thermal conductivity of various materials measured by the FDTR/TDTR versus previously found literature thermal conductivity.

We can note substantial agreement on the whole thermal conductivity range, which shows the capability of this sensor to identify thermal conductivities on a range of three decades.

We must now ensure that this kind of measurements will allow the distinction between a purely diffusive regime from a Lévy dynamics regime.

Experimental evidence of thermal superdiffusive transport

In this last section, we have investigated the expected superdiffusive behavior in a 2-µm thick InGaAs alloy sample. The study of this quasi-ballistic thermal behavior was carried out in several steps.

Firstly, we measured the phase spectral response of the sample studied using the FDTR/TDTR thermal sensor. Then we applied two optimizations to the experimental signal to describe the thermal response. The first optimization was performed using the purely diffusive Fourier one temperature Model (Fourier 1TM) and the second using the superdiffusive Lévy model. If the studied sample solely exhibits a pure thermal diffusive behavior, the two temperature models, 1TM and Lévy, should converge and identify identical thermal properties (α should converge to 2). However, for materials in which a superdiffusive regime exists, 1TM should not be able to correctly describe the spectral phase response and therefore should not be able to identify consistent values.

The sample studied is the $In_{0.53}Ga_{0.47}As$ alloy, in which, according to the literature[7,14], there is a frequency dependence of the thermal conductivity, indicating the presence of a pronounced Levy-Fourier transition. Here we show the ability of the FDTR/TDTR sensor to detect this superdiffusive regime.

The structure of the sample consisted of a 2000-nm thick InGaAs layer deposited on an InP substrate with a 70-nm thick aluminum transducer deposited on top. Figure 6 shows the multilayer structure of this sample with the thermal properties essential for its modeling, the known values being taken from the literature[50]. The properties of the aluminum transducer and all fixed parameters are summarized in Fig. 6. The value of the thermal resistance $R_{InGaAs/InP}$ between InGaAs layer and substrate has no significant effect due to the low sensitivity of the response to it since the InGaAs thickness is larger than the diffusion length in the frequency range of interest.

The 1TM optimization was performed with two free parameters, the thermal conductivity of InGaAs (k_{InGaAs}) and the thermal resistance between the Al transducer and the InGaAs layer ($R_{Al/InGaAs}$). For the Lévy model, which describes the heat in a semi-infinite medium over which a transducer is placed, the InGaAs layer was considered as a substrate. In addition to the thermal conductivity of InGaAs (k_{InGaAs}) and the thermal resistance ($R_{Al/InGaAs}$), optimization with this thermal model allows the identification of two other parameters, namely the super-diffusion exponent (α) and the characteristic transition length (u_{BD}).

Figure 7 shows the measured spectral phase response of the Al/$In_{0.53}Ga_{0.47}As$/InP sample on which two optimizations are performed, the first with the classical Fourier-1TM and the second with the Lévy model. Raw data for amplitude and phase of the thermal response are shown in Supplementary Fig. S5.1. We can immediately see the inability of the Fourier-1TM model to describe the entire frequency response of the sample. The purely diffusive model does not fit the experimental response, especially with a frequency range from 200 kHz to 200 MHz. However, the model fit is adequate at high frequencies (200 MHz to 10 GHz) where the thermal response is sensitive to the Al transducer effect. This is also the case at low frequencies (below 200 kHz) where the response is sensitive to the thermal effect of the InP substrate. Therefore, the discrepancy only exists in the range where the response is sensitive to the InGaAs layer. The parameters identified by this 1TM optimization are 3.4 W.m^{-1}.K^{-1} for the k_{InGaAs} and 11.8 nK.m^2.W^{-1} for the $R_{Al/InGaAs}$. The thermal conductivity is 50% lower than what would be expected, while the thermal resistance is 50% higher than literature values.

The same figure also shows the optimization performed by the semi-infinite Lévy model. In contrast to the Fourier−1TM, the Lévy gives a more accurate fit to the thermal response above the 200 kHz frequency. The best optimization is obtained with values of $\alpha = 1.7 \pm 0.1$, $u_{BD} = 3.5 \pm 1.6$ µm for, $k_{InGaAs} = 5.9 \pm 0.4$ W.m^{-1}.K^{-1} and $R_{Al/InGaAs} = 5.1 \pm 3.5$ nK.m^2.W^{-1} Error bars are calculated by propagating uncertainties in the fixed thermophysical parameters, mainly the Al thickness (±5 nm) and rms laser spot size (±5%), and 10% for the all the others taken from the literature.

These identified values are in perfect agreement with the theory and measurements found in the literature[7,14]. This implies that the model was able to describe the thermal frequency response of InGaAs while maintaining a frequency-independent thermal transport of the material.

Consequently, the failure of the purely diffusive Fourier−1TM to describe the thermal response is in agreement with the theoretical simulations by Vermeersch[14,19] which predict the existence of the superdiffusive regime in the InGaAs alloy.

Conclusions

A superdiffusive thermal behavior, distinct from conventional Brownian motion, is expected in some particular semiconductors. Indeed, for most of

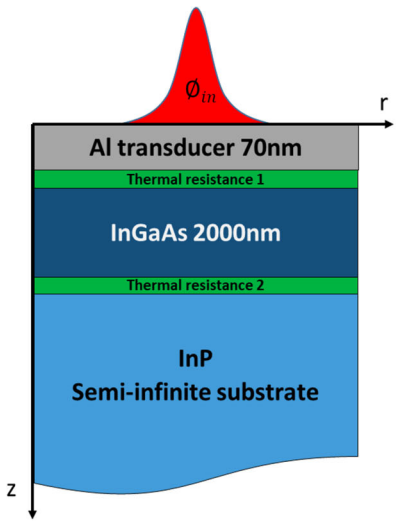

		Thermal parameters	
		Thermal resistance 1	$R_{Al/InGaAs}$=? nK.m^2/W
Layer	InGaAs	Thickness	d_{InGaAs}=2000 nm
		Thermal conductivity	k_{InGaAs}=? W/m/K
		Specific heat capacity	ρC_{InGaAs}=1.6 $MJ/m^3/K$
		Thermal resistance 2	$R_{InGaAs/InP}$=1 nK.m^2/W
Substrate	InP	Thermal conductivity	k_{InP}=65 W/m/K
		Specific heat capacity	ρC_{InP}=1.49 $MJ/m^3/K$

Fig. 6 | Thermal model. Schematic description of the Al/InGaAs/InP sample and table summarizing the thermal properties used for the modeling.

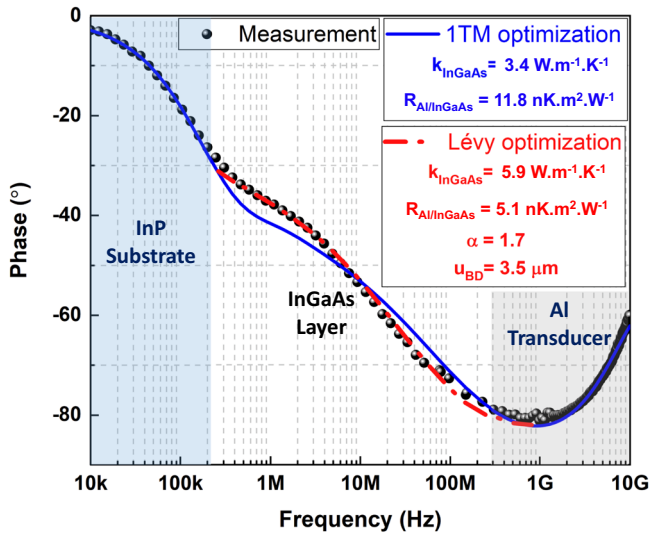

Fig. 7 | Optimization on InGaAs phase response and experimental evidence of superdiffusive transport. Spectral phase of the thermal response measured for Al/$In_{0.53}Ga_{0.47}As$/InP sample. Black dots represent the experimental response. The blue continuous line shows the theoretical response adjusted by the Fourier-1TM. The red dashed line shows the theoretical response adjusted by the Lévy model. The spectral modulus is shown in Supplementary Fig. S5.1.

these materials, the transition between both purely diffusive and super-diffusive regimes was theoretically predicted in a frequency range between 1 MHz and 1 GHz. However, pump-probe experimental benches work either at low frequencies (FDTR) with an upper limit around a few tens of MHz or at high frequencies (TDTR) with a lower frequency limit and frequency resolution around 76 MHz corresponding to the laser repetition rate.

We have proposed to merge both setups to reach an ultrabroad bandwidth covering a frequency range from 10 kHz to 100 GHz. The ability of this experimental set-up to evaluate the thermal conductivity of materials over three decades has been demonstrated.

In addition, by comparing the classical Fourier-1TM with the Lévy model, we have shown that, even if the transducer (compulsory in pump-probe experiments), evens out the temperature distribution and masks non-diffuse effects when viewed from the sample surface, super-diffusion is still visible from above the transducer over two decades around 10 MHz, in particular in the phase signal.

Finally, experimental pump-probe measurements on an InGaAs alloy sample have highlighted the existence of the superdiffusive regime in the InGaAs alloy. As a perspective to this work, investigations of phonon transport mechanisms as a function of temperature can be interesting to address a broad range of materials. Going to lower temperatures can provide new insights above transitions such as: Levy flights, hydrodynamic and ballistic transport.

Methods

In this paper, we have used heterodyne or asynchronous TDTR[32–34] which consists in using two laser sources respectively delivering pump and probe pulse trains at different repetition frequencies. The signal is then measured at the beating frequency (see Supplementary Information S1). The latter must be electronically stabilized. Consequently, all mechanical translation devices are no longer required, and their inherent limitations cease to exist. The signal processing from the raw time-dependent data to the frequency domain signal is based on a classical Fourier transform and is detailed in ref. 34. The benefits of this approach are numerous in comparison with classical TDTR[35]: i) the acquisition time reduced by several orders of magnitude, ii) an extension of several decades of the temporal range studied, iii) no change in the size of the laser spot on the sample, iv) the disappearance of unstable pointing, v) the elimination of noise due to the translation of the plates, vi) the access to imaging techniques with picosecond time resolution. The spectral bandwidth typically extends from 76 MHz to 1 THz[36] limited on one hand by the repetition rate of the pump laser and on the other by the spectral extension of the laser pulse.

In the FDTR technique[37–40], the thermoreflectance signal is measured with respect to the modulation frequency of the pump beam amplitude while the probe beam is a CW laser (see Supplementary Information S1). The FDTR method can be implemented with two continuous wave lasers. The intensity of the pump beam is modulated either directly by a function generator or by passing the laser beam through an electro-optic modulator. For both modulation methods, the modulation frequency range is generally swept from a few kHz up to a hundred MHz. The pump and probe beams are focused on the sample surface with the same objective. After reflection, the intensity of the probe is detected by a photodiode, and a lock-in amplifier synchronized on the pump frequency is used to measure the phase and magnitude of the thermoreflectance signal from the reflected probe beam intensity.

Associated content

Supplementary information: The TDTR and FDTR optical benches are described in Supplementary Information S1. In Supplementary

Information S2, we show that, in the frequency range where super-diffusion occurs, the non-equilibrium electrons do not contribute to the thermoreflectance signal. Supplementary Information S3 is dedicated to the model sensitivity in order to identify thermal parameters simultaneously on a wide frequency range. Supplementary Information S4 shows the phase frequency response on 5 materials with thermal conductivities ranging from 0.2 to 16.4 $W.m^{-1}.K^{-1}$ in addition to the silicon sample (135 $W.m^{-1}.K^{-1}$) detailed in the main text. Supplementary Information S5 shows the raw data amplitude and phase of the spectral thermal response on InGaAs.

Data availability

The raw data in support of most of the quantitative figures reported in this work are reported in the Supplementary Information. All of the other data are available from the corresponding author upon reasonable request.

Received: 6 March 2024; Accepted: 11 July 2024;
Published online: 20 July 2024

References

1. Perri, S., Zimbardo, G., Effenberger, F. & Fichtner, H. Parameter estimation of superdiffusive motion of energetic particles upstream of heliospheric shocks. *Astron. Astrophys.* **578**, A2 (2015).
2. Molina-Garcia, D. et al. Crossover from anomalous to normal diffusion: truncated power-law noise correlations and applications to dynamics in lipid bilayers. *N. J. Phys.* **20**, 103027 (2018).
3. Ziabari, A. et al. Full-field imaging of quasiballistic crosstalk reduction in nanoscale devices. *Nat. Comm.* **9**, 255 (2018).
4. Beardo, A. et al. Hydrodynamic thermal transport in silicon at temperatures ranging from 100 to 300K. *Phys. Rev. B* **105**, 165303 (2022).
5. Beardo, A. et al. A general and predictive understanding of thermal transport from 1D- and 2D-confined nanostructures: theory and experiment. *ACS Nano* **15**, 13019 (2021).
6. Beardo, A., Hennessy, M. G., Sendra, L., Camacho, J., Myers, T. G., Bafaluy, J. & Alvarez, F. X. Phonon hydrodynamics in frequency-domain thermoreflectance experiments. *Phys. Rev. B* **101**, 075303 (2020).
7. Koh, Y. K. & Cahill, D. G. Frequency dependence of the thermal conductivity of semiconductor alloys. *Phys. Rev. B* **76**, 075207 (2007).
8. Bera, C., Mingo, N. & Volz, S. Marked Effects of Alloying on the Thermal Conductivity of Nanoporous Materials. *Phys. Rev. Lett.* **104**, 115502 (2010).
9. Minnich, A. J. et al. Thermal Conductivity Spectroscopy Technique to Measure Phonon Mean Free Paths. *Phys. Rev. Lett.* **107**, 095901 (2011).
10. Regner, K. T. et al. Broadband phonon mean free path contributions to thermal conductivity measured using frequency domain thermoreflectance. *Nat. Commun.* **4**, 1640 (2013).
11. Siemens, M. E. et al. Quasi-ballistic thermal transport from nanoscale interfaces observed using ultrafast coherent soft X-ray beams. *Nat. Mater.* **9**, 26–30 (2010).
12. Zeng, L. et al. Measuring Phonon Mean Free Path Distributions by Probing Quasi-ballistic Phonon Transport in Grating Nanostructures. *Sci. Rep.* **5**, 17131 (2015).
13. Johnson, J. A. et al. Direct Measurement of Room-Temperature Nondiffusive Thermal Transport Over Micron Distances in a Silicon Membrane. *Phys. Rev. Lett.* **110**, 025901 (2013).
14. Vermeersch, B., Carrete, J., Mingo, N. & Shakouri, A. Superdiffusive heat conduction in semiconductor alloys. I. Theoretical foundations. *Phys. Rev. B* **91**, 085202 (2015).
15. Shlesinger, M. F., Klafter, J. & Zumofen, G. Above, below and beyond Brownian motion. *Am. J. Phys.* **67**, 1253–1259 (1999).
16. Yao, F. et al. Experimental Evidence of Superdiffusive Thermal Transport in $Si_{0.4}Ge_{0.6}$ Thin Films. *Nano Lett.* **22**, 6888–6894 (2022).
17. Klafter, J., Blumen, A. & Shlesinger, M. F. Stochastic pathway to anomalous diffusion. *Phys. Rev. A* **35**, 3081 (1987).
18. Metzler, R. & Klafter, J. The random walk's guide to anomalous diffusion: a fractional dynamics approach,. *Phys. Rep.* **339**, 1–77 (2000).
19. Vermeersch, B., Mohammed, A. M. S., Pernot, G., Koh, Y. R. & Shakouri, A. Superdiffusive heat conduction in semiconductor alloys. II. Truncated Lévy formalism for experimental analysis. *Phys. Rev. B* **91**, 085203 (2015).
20. Koponen, I. Analytic approach to the problem of convergence of truncated Lévy flights towards the Gaussian stochastic process,. *Phys. Rev. E* **52**, 1197–1199 (1995).
21. Paddock, C. A. & Eesley, G. L. Transient thermoreflectance from thin metal films. *J. Appl. Phys.* **60**, 285 (1986).
22. Pernot, G. et al. Precise control of thermal conductivity at the nanoscale through individual phonon-scattering barriers. *Nat. Mater.* **9**, 491 (2010).
23. Juvé, V. et al. Cooling dynamics and thermal interface resistance of glass-embedded metal nanoparticles. *Phys. Rev. B* **80**, 195406 (2009).
24. Sun, C.-K., Vallée, F., Acioli, L., Ippen, E. P. & Fujimoto, J. G. Femtosecond investigation of electron thermalization in gold. *Phys. Rev. B* **48**, 12365 (1993).
25. Sood, A. et al. Quasi-ballistic thermal transport across MoS_2 thin films. *Nano Lett.* **19**, 2434 (2019).
26. Xiao, P. et al. Anisotropic thermal conductivity of crystalline layered $SnSe_2$. *Nano Lett.* **21**, 9172 (2021).
27. Chavez-Angel, E. et al. Engineering heat transport across epitaxial lattice-mismatched van der Waals heterointerfaces. *Nano Lett.* **23**, 6883 (2023).
28. Decremps, F., Belliard, L., Perrin, B. & Gauthier, M. Sound Velocity and Absorption Measurements under High Pressure Using Picosecond Ultrasonics in a Diamond Anvil Cell: Application to the Stability Study of AlPdMn. *Phys. Rev. Lett.* **100**, 035502 (2008).
29. Norris, P. M. et al. Femtosecond pump–probe nondestructive examination of materials. *Rev. Sci. Instrum.* **74**, 400 (2003).
30. Crut, A., Maioli, P., Del Fatti, N. & Vallée, F. Acoustic vibrations of metal nano-objects: Time-domain investigations. *Phys. Rep.* **549**, 1 (2015).
31. Ezzahri, Y., Grauby, S., Dilhaire, S., Rampnoux, J.-M. & Claeys, W. Cross-plan Si/SiGe superlattice acoustic and thermal properties measurement by picosecond ultrasonics,. *J. Appl. Phys.* **101**, 013705 (2007).
32. d'Acremont, Q. et al. High-throughput heterodyne thermoreflectance: Application to thermal conductivity measurements of a Fe–Si–Ge thin film alloy library. *Rev. Sci. Instrum.* **88**, 074902 (2017).
33. Jiang, P., Qian, X. & Yang, R. Tutorial: Time-domain thermoreflectance (TDTR) for thermal property characterization of bulk and thin film materials. *J. Appl. Phys.* **124**, 161103 (2018).
34. Dilhaire, S., Pernot, G., Calbris, G., Rampnoux, J. M. & Grauby, S. Heterodyne picosecond thermoreflectance applied to nanoscale thermal metrology. *J. Appl. Phys.* **110**, 114314 (2011).
35. Grauby, S., Vidal Montes, B., Zenji, A., Rampnoux, J.-M. & Dilhaire, S. How to Measure Hot Electron and Phonon Temperatures with Time Domain Thermoreflectance Spectroscopy? *ACS Photonics* **9**, 3734 (2022).
36. Zenji, A., Rampnoux, J. M., Grauby, S. & Dilhaire, S. Ultimate-resolution thermal spectroscopy in time domain thermoreflectance (TDTR). *J. Appl. Phys.* **128**, 065106 (2020).
37. Rosencwaig, A., Opsal, J., Smith, W. L. & Willenborg, D. L. Detection of thermal waves through optical reflectance. *Appl. Phys. Lett.* **46**, 1013 (1985).
38. Forget, B. C., Barbereau, I. & Fournier, D. Electronic diffusivity measurement in silicon by photothermal microscopy. *Appl. Phys. Lett.* **69**, 11107 (1996).

39. Schmidt, A. J., Cheaito, R. & Chiesa, M. Characterization of thin metal films via frequency-domain thermoreflectance. *J. Appl. Phys.* **107**, 024908 (2010).
40. Wang, L., Cheaito, R., Braun, J. L., Giri, A. & Hopkins, P. E. Thermal conductivity measurements of non-metals via combined time- and frequency-domain thermoreflectance without a metal film transducer. *Rev. Sci. Instrum.* **87**, 094902 (2016).
41. Carslaw, H. C. & Jaeger, J. C. *Conduction of heat in solids* (Oxford University Press, 1959).
42. Maillet, D., André, S., Batsale, J. C., Degiovanni, A., & Moyne, C. *Thermal quadrupoles: solving the heat equation through integral transforms* (John Wiley and Sons, 2000).
43. Wilson, R. B. & Cahill, D. G. Anisotropic failure of Fourier theory in time-domain thermoreflectance experiments. *Nat. Comm.* **5**, 5075 (2014).
44. Shanks, H. R., Maycock, P. D., Sidles, P. H. & Danielson, G. C. Thermal Conductivity of Silicon from 300 to 1400°K,. *Phys. Rev.* **130**, 1743 (1963).
45. Glassbrenner, C. J. & Slack, G. A. Thermal Conductivity of Silicon and Germanium from 3°K to the Melting Point. *Phys. Rev.* **134**, A1058 (1964).
46. Cahill, D. G. & Allen, T. H. Thermal conductivity of sputtered and evaporated SiO2 and TiO2 optical coatings. *Appl. Phys. Lett.* **65**, 309 (1994).
47. Burmistova, P. V. et al. Thermoelectric properties of epitaxial ScN films deposited by reactive magnetron sputtering onto MgO(001) substrates. *J. Appl. Phys.* **113**, 153704 (2013).
48. Tureson, N. et al. Reduction of the thermal conductivity of the thermoelectric material ScN by Nb alloying. *J. Appl. Phys.* **122**, 025116 (2017).
49. Oh, D.-W., Ko, C., Ramanathan, S. & Cahill, D. G. Thermal conductivity and dynamic heat capacity across the metal-insulator transition in thin film VO_2. *Appl. Phys. Lett.* **96**, 151906 (2010).
50. Maycock, P. D. Thermal conductivity of silicon, germanium, III–V compounds and III–V alloys. *Solid State Electron.* **10**, 161 (1967).

Acknowledgements

This work was performed in the framework of the Spiderman ANR project (ANR−18-CE42-0006-03) funded by the French Agence Nationale de la Recherche and of the CHARTS project (2019-1R1M04) funded by the Regional Council of Nouvelle Aquitaine.

Author contributions

Ahmad Zenji: measurements, data analysis, and writing - reviewing; Gilles Pernot: sample production, and writing - reviewing; David Lacroix: writing - reviewing; Jean-Michel Rampnoux: data analysis, simulations; Olivier Bourgeois: writing - reviewing; Stéphane Grauby: conceptualization, methodology, data analysis, and writing – original draft; Stefan Dilhaire: conceptualization, methodology, data analysis, and writing – original draft.

Competing interests

The authors declare no competing interests.

Additional information

Supplementary information The online version contains supplementary material available at https://doi.org/10.1038/s43246-024-00572-7.

Correspondence and requests for materials should be addressed to Stéphane Grauby or Stefan Dilhaire.

Peer review information *Communications Materials* thanks Juan Reparaz, Alexandros El Sachat and the other, anonymous, reviewer(s) for their contribution to the peer review of this work. Primary Handling Editors: Klaas-Jan Tielrooij and Aldo Isidori. A peer review file is available.